Near-Infrared Plasmon-Boosted Heat/Oxygen Enrichment for Reversing Rheumatoid Arthritis with Metal/Semiconductor Composites

Shasha Wang,[†,‡] *Ronghe Chen,*[‡] *Qian Yu,*[‡] *Wenchao Huang,*[‡] *Puxiang Lai,*[§] *Jianxin Tang,**[,†] *and Liming Nie**[,‡]

[†]Hunan Key Laboratory of Biomedical Nanomaterials and Devices, Hunan University of Technology, Zhuzhou 412007, P. R. China

[‡]State Key Laboratory of Molecular Vaccinology and Molecular Diagnosis & Center for Molecular Imaging and Translational Medicine, School of Public Health, Xiamen University, Xiamen 361102, P. R. China

[§]Department of Biomedical Engineering, The Hong Kong Polytechnic University, Hong Kong SAR, China

KEYWORDS: plasmonic phototherapy, enhanced catalytic performance, oxygen generation, rheumatoid arthritis, combined therapy

ABSTRACT: Rheumatoid arthritis (RA) is an autoimmune disease that often causes progressive joint dysfunction, even disability and death in severe cases. The radical improvement of inflammatory cell infiltration and the resulting disorder in oxygen supply is a fire-new therapeutic direction for RA. Herein, a near-infrared-absorbing

metal/semiconductor composite, polyethylene glycol-modified ceria shell coated gold nanorod (Au@CeO_2), is fabricated for topical photothermal/oxygen-enriched combination therapy for RA in a mouse model. Upon laser irradiation, the photothermal conversion of Au@CeO_2 is exponentially enhanced by the localized surface plasma resonance-induced light focusing. The elevated temperature can not only remarkably obliterate hyperproliferative inflammatory cells gathered in diseased joints, but also vastly increase the catalase-like activity of ceria to accelerate the decomposition of H_2O_2 to produce much oxygen, which relieves hypoxia. Significantly, RA-induced lesions are improved, and the expression of pro-inflammatory cytokines and hypoxia-inducible factor is effectively repressed under the cooperation of heat and oxygen. Overall, the core/shell structured Au@CeO_2 is a promising nanotherapeutic platform that can well realize light-driven heat/oxygen enrichment to completely cure RA from the perspective of pathogenesis.

Rheumatoid arthritis (RA) characterized by chronic synovitis and cartilage destruction is a widespread autoimmune and systemic inflammatory disease that results in long-term synovitis, progressive joint dysfunction, disability, and increased mortality.[1,2] The precise origin of RA onset remains elusive because of complicated pathogenesis.[3] In clinic, the principally therapeutic approach for RA is disease-modifying anti-rheumatic drugs (DMARDs), especially methotrexate (MTX), one of the most widely used DMARD. However, because of short half-life and poor bioavailability, patients need high dose and frequent administration which bring

damage to normal tissues.[4-6] The inflammatory responses in the RA joints depend greatly on activated innate effector cells such as macrophages, neutrophils, dendritic cells, T and B lymphocytes, and mast cells, which infiltrate into the diseased joint after unwanted immune responses, bringing about the serious destruction of articular bone and cartilage.[7-9] Furthermore, the aggregated inflammatory cells secrete inflammatory cytokines, cell adhesion molecules, chemokines and matrix metalloproteinases, which are associated with synovial hyperplasia, massive angiogenesis, cartilage matrix disintegration, and bone destruction.[10-12] Thus, The elimination of hyperproliferative inflammatory cells is deemed to be the key for RA therapy.

Hypoxia is one of the typical characteristics of inflammatory joints, which is caused by the increased oxygen demand of overgrown heterogeneous effector cells and vascular dysfunction in diseased joints.[13] Commonly, hypoxia induces the production of some undesirable inflammatory metabolites such as reactive oxygen species (ROS) and reactive nitrogen oxygen species (RNOS) which can expedite the mutagenesis and metastasis of inflammatory cells, giving rise to severe synovitis and bone erosion.[14-17] Moreover, hypoxia up-regulates hypoxia-inducible factor (HIF-1α) expression in RA which is reported to induce synovial inflammation of the joints and unreversible destruction of cartilage/bone.[13,18] Therefore, hypoxia relief can be considered as a potential target for the treatment of RA.

To date, catalase-like nanomaterials have been developed to generate oxygen by scavenging ROS in situ under H_2O_2-rich hypoxic environment, improving the

treatment efficacy.[19-23] For instance, MnO_2-related materials exhibit catalase-like activity that can trigger the decomposition of endogenous H_2O_2 to produce oxygen, modulating tumor hypoxia microenvironment to fulfill a remarkably enhanced photodynamic therapy (PDT) efficacy.[24-27] Additionally, some studies have found that the photothermal-based temperature rise formed on near-infrared (NIR)-absorbing nanomaterials can enhance the burst release of oxygen to greatly alleviate the state of oxygen deficiency.[21,28,29] Moreover, such local high temperature itself leads to widespread cell death in the lesion site.[30-34] Based on these research facts, we assume that the effective combination of photothermal therapy and oxygen-enriched therapy is possible to radically reverse RA without side effects.

Recently, ceria (CeO_2) nanoparticles have been extensively investigated due to its superior catalytic performance for eliminating ROS and producing oxygen in varied inflammatory diseases.[35-37] The unique regenerative antioxidant property of CeO_2 is closely related to the reversible switch between two oxidation states (Ce^{3+} and Ce^{4+}) which appear on the surface of nanoparticles.[38-40] Gold nanorods (AuNRs), which are characterized by an inherently high absorbance-to-scattering ratio, efficient photothermal conversion, and easily tunable localized surface plasma resonance (LSPR) band for NIR absorption, are considered as a notable candidate for plasmonic photothermal therapy (PPT).[30, 41-44] To achieve the above proposed combination therapy strategy for RA, we designed a polyethylene glycol (PEG) modified core-shell nanostructure of gold nanorod coating with ceria (Au@CeO_2) (Scheme 1). Under NIR laser irradiation, enhanced LSPR improves the photothermal effect of

Au@CeO_2 to effectively kill the inflammatory cells gathered in RA joints and to augment CeO_2 catalytic effect on H_2O_2 to accelerate oxygen generation. Meanwhile, electron flows generated by the LSPR of AuNRs are captured by CeO_2 to accelerate the occurrence of Ce^{4+} to Ce^{3+} transformation which as well heightens H_2O_2 decomposition and oxygen production. In other words, we expect that AuNR and CeO_2 will exhibit a synergistic effect on photothermal destruction and oxygen generation, which can cure RA with a relatively low NPs concentration.

In our work, Au@CeO_2 was firstly fabricated and then applied as a nanotherapeutic reagent to photothermal/oxygen-enriched combination therapy in a preclinical classic RA mouse model. We systematically investigated the properties of Au@CeO_2 nanoparticles *in vitro* and *in vivo*, including PPT effect and the ability of generating oxygen. Additionally, there is still a lack of accurate and reliable tools to detect oxygen levels in the articular cavity. Photoacoustic imaging (PAI) possesses rich optical contrast, high ultrasonic spatial resolution, and deep penetration depth to offer structural, functional, and molecular images for disease diagnosis and therapeutic monitoring *in vivo*.[45-47] Here, we used PA signals from hemoglobin oxygen saturation (sO_2) to monitor the levels of oxygen produced in the blood of hypoxic ankle joints. This study will not only promote the application of CeO_2-based nanomaterials in RA treatment, but also provide guidance for the design of other nanosystems to treat intractable autoimmune diseases.

RESULTS AND DISCUSSION

Preparation and Characterization of Au@CeO_2 Nanoparticles. To synthesize Au@CeO_2 nanoparticles, uniform sized AuNRs were prepared as seeds using the silver ion-assisted seed-mediated method.[48-50] The transmission electron microscopy (TEM) image of AuNRs (Figure 1a) showed favorable dispersibility. AuNRs served as the cores were stabilized by cetyltrimethylammonium bromide (CTAB) in aqueous solutions. Then, the Au@CeO_2 core-shell nanostructures were developed by reducing the $Ce(NO_3)_3$ precursor with hydrazine hydrate on the synthesized AuNRs seeds. The conjugation of ceria to AuNRs was confirmed by scanning electron microscopy (SEM) and TEM of Au@CeO_2 (Figure 1b,c). The CeO_2 shell was relatively uniform wrapped on the surface of AuNR in all core@shell nanostructures. TEM image taken at the end of a single Au@CeO_2 nanostructure (Figure 1d) indicated the interface between AuNR and CeO_2. The white dashed line intuitively showed the coverage of CeO_2 to AuNR (Figure 1e). Through high-angle annular dark-field scanning transmission electron microscopy (HAADF-STEM) image (Figure 1f), we clearly observed elemental maps of Au, Ce, and O, respectively, on the representative individual nanostructure, corroborating the successful preparation of Au@CeO_2. Moreover, inductively coupled plasma mass spectrometry (ICP-MS) analysis validated that the mass ratio of gold to ceria in the prepared Au@CeO_2 nanostructure was 1/2.

As confirmed by ultraviolet−visible (UV−vis) spectroscopy (Figure 1g), the Au@CeO_2 had a sharp extinction peak located at 810 nm, which accounted for surface plasmon resonance absorption of AuNRs. The modification of PEG was used to endow Au@CeO_2 with good water solubility and biocompatibility. The particle

diameter of Au@CeO_2 was assessed using dynamic light scattering (DLS) (Figure 1h). The final hydrodynamic particle size increased from 45.6 ± 1.5 nm of AuNR to 102.8 ± 2.3 nm of PEGylated Au@CeO_2, further indicating the successful coating of CeO_2 on the surface of AuNRs. X-ray diffraction (XRD) patterns were employed to investigate the crystal phases of Au@CeO_2 nanostructures (Figure 1i). It remarkably exhibited two sets of diffraction peaks which matched well with the crystal planes of AuNR and CeO_2. As observed from Figure 1e, as-prepared Au@CeO_2 crystalline had an interplanar spacing of 0.312 nm, which corresponded to the (111) plane of the cubic CeO_2 phase.

Plasmonic Photothermal and Photoacoustic Properties of Au@CeO_2 Nanoparticles. As shown in Figure 1g, the Au@CeO_2 displayed the most pronounced absorption at 810 nm, which encourages us to further investigate their potential in plasmonic photothermal effect. In the case of same external conditions (wavelength: 808 nm, laser energy: 1 W cm^{-2}, irradiation time: 5 min, concentration: 200 μg mL^{-1}), we recorded the temperature variations of different solutions. Compared with PBS, CeO_2, and AuNR solutions, the temperature of the Au@CeO_2 solution increased dramatically and reached a plateau about 57.6 °C in 5 min (Figure 2a). Infrared (IR) camera recorded the maximum temperature of all samples after laser irradiation (Figure 2c), intuitively indicating better photothermal properties of Au@CeO_2. Furthermore, the photothermal conversion efficiency was calculated to be 33.7% (Figure S1) on the basis of the previously reported method.[51] In addition, the rise of temperature showed a time-dependent and concentration-dependent tendency (Figure

2b). To evaluate the photothermal stability of Au@CeO_2, five cycles of reversible photothermal heating and cooling experiments were carried out (Figure S2), the results showed that repeated light irradiation had not any significant change in the photothermal performance of Au@CeO_2.

Encouraged by the intense NIR absorption, we further assessed the potential of Au@CeO_2 as a strong photoacoustic (PA) agent. PA properties of AuNR, CeO_2 and Au@CeO_2 were examined (Figure 2d). Notably, the result showed that, compared with other two groups, Au@CeO_2 exhibited much higher signal intensities even at a concentration as low as 25 μg mL^{-1}, which coincided with the quantitative results shown in Figure 2e.

Subsequently, after intra-articular injection with PBS, AuNR, and Au@CeO_2, PA signal intensity in the RA mice was captured to track the distribution of NPs (Figures S3 and S4). For the AuNR and Au@CeO_2 injected groups, the strongest PA intensities were obtained at the beginning because of directly injecting into the articular cavity. Then the signal intensities gradually decreased and reached a plateau to the original level on day 15. Moreover, the aggregation of Au@CeO_2 in articular cavity indicated a superior PA signal compared with AuNR, implying its advantage as an ideal contrast agent for PAI *in vivo*. By contrast, the PA signal in the control group injected with PBS exhibited little fluctuation over time. Additionally, representative cube, transverse and sagittal views of 3D reconstruction PA images of the arthritis paw on day 7 (Figure S5) also intuitively reflected the movement of Au@CeO_2. The experimental results demonstrated that PAI combined with Au@CeO_2 was an accurate

and straightforward method for monitoring the accumulation and spread process of the NPs inside the inflammatory claws.

Oxygen Generation of Au@CeO_2 Nanoparticles. Previous studies had preliminarily reported that CeO_2 nanoparticles possessed a notable catalase-like activity in the decomposition of H_2O_2 into oxygen and H_2O.[52,53] We verified that surface modified Au@CeO_2 still had a superior ability of decomposing H_2O_2 to generate oxygen. To study the ability of Au@CeO_2 to generate oxygen, the catalytic performances of AuNR, CeO_2 and Au@CeO_2 were investigated in the presence or absence of NIR laser. As shown in Figure 2f, 82.7% of H_2O_2 was decomposed by Au@CeO_2 in 1 h after laser exposure compared with 10.4% and 45.2% of H_2O_2 decomposition by AuNR and CeO_2, respectively. Nevertheless, the H_2O_2 decomposition of Au@CeO_2 without laser irradiation was barely 30.9% at the same concentration, certificating the prominently enhanced catalytic effect of Au@CeO_2 when exposed to the laser. Correspondingly, enhanced dissolved oxygen value and obvious oxygen bubbles were served to testify the capacity of Au@CeO_2 to rapidly produce oxygen in the presence of laser (Figure 2g,h and Figure S1b). These results manifested that Au@CeO_2 performed enhanced catalytic effect in decomposing H_2O_2 to produce oxygen under laser exposure.

In addition, we further determined the mutual cooperation by blending AuNR and CeO_2. The results showed that the mixture of AuNR and CeO_2 rarely exhibited a promotional effect on H_2O_2 decomposition and oxygen generation compared with Au@CeO_2 with laser irradiation (Figure S6), suggesting that the interaction between

core and shell of $Au@CeO_2$ could significantly enhance its antioxidant properties. Subsequently, six groups at different concentrations ranging from 0 to 200 μg mL^{-1} were applied to reliably evaluate the catalytic capability of $Au@CeO_2$ under laser irradiation. We observed that the H_2O_2 decomposition and oxygen generation were positively correlated with the concentration of $Au@CeO_2$ (Figure S7).

Cytotoxicity and PPT of $Au@CeO_2$ Nanoparticles *In Vitro*. *In vitro* experiments were performed using a murine macrophage cell line RAW 264.7 generally utilized as a cellular model in RA researches. We first evaluated cytotoxicity according to a standard 3-(4,5-Dimethylthiazol-2-yl)-2,5diphenyltetrazolium bromide (MTT) assay (Figure S8). After 24 h and 48 h of incubation with $Au@CeO_2$, no significant cytotoxicity was observed until the concentration up to 200 μg mL^{-1}, suggesting their good biocompatibility and lower toxicity.

Then, we explored the PPT effect of $Au@CeO_2$ on lipopolysaccharide (LPS)-induced inflammatory RAW 264.7 cells. Concentration-dependent cytotoxicity was inspected using MTT assay after 5 min irradiation at 808 nm (1 W cm^{-2}). As shown in Figure 3b, NIR-irradiated cells incubated with $Au@CeO_2$ displayed a more pronounced cell growth inhibition than that of AuNR, which was prompted by enhanced local hyperthermia. The IC_{50} value for the $Au@CeO_2$ group was approximately 32.7 μg mL^{-1} while was about 55.2 μg mL^{-1} for AuNR group, confirming that the $Au@CeO_2$ possessed a preferable PPT efficacy. Furthermore, to visually evaluate PPT *in vitro*, calcein AM (staining live cells, green fluorescence) and propidium iodide (PI, staining dead cells, red fluorescence) were utilized to

qualitatively verify the cellular status (Figure 3a). Confocal laser scanning microscopy (CLSM) showed that intense green fluorescence was observed in cells treated by NPs or NIR alone, indicating highly biocompatibility of NPs and no harm to cells in only laser scenario. Upon laser irradiation, strong red fluorescence was obviously observed in Au@CeO_2-incubated cells while both green and red fluorescence appeared in AuNR-incubated cells, illustrating that the Au@CeO_2 had a better PPT efficiency in LPS-induced inflammatory cells.

Enhanced Hydrogen Peroxide Scavenging and Pro-Inflammatory Inhibition Effect of Au@CeO_2 Nanoparticles *In Vitro*. Abnormal metabolism of aggregated inflammatory cells may cause the increase of ROS generation inside the inflammatory cells. Hence, inflammation can be alleviated to some extent by scavenging ROS. To evaluate ROS scavenging capacity of Au@CeO_2 *in vitro*, an intracellular H_2O_2 assay kit was used to measure intracellular H_2O_2 levels (Figure 3c). After laser irradiation for 5 min, LPS-induced RAW 264.7 cells pretreated with CeO_2 and Au@CeO_2 were incubated with 100 μM H_2O_2 for 1 h. Then we appraised intracellular H_2O_2 level by fluorescence intensity. As shown in Figure 3c, compared with cells treated with either laser-irradiated CeO_2 or laser alone, cells treated with Au@CeO_2 and laser exposure exhibited faint green fluorescence. The result unraveled that Au@CeO_2 interacted with laser showed an excellent performance in efficiently decomposing intracellular H_2O_2, demonstrating the enhanced ROS scavenging, which was in accordance with the previous results. Correspondingly, quantitative results confirmed a significant difference of fluorescence intensity between Au@CeO_2-laser treated cells and other

control cells (Figure 3d).

Subsequently, we measured the intracellular levels of pro-inflammatory cytokines (TNF-α, IL-6, and IL-1β) by enzyme linked immunosorbent assay (ELISA) analysis. We first evaluated the levels of pro-inflammatory cytokines in the LPS-induced RAW 264.7 cells and normal cells respectively, confirming that there was a significant difference between two groups ($P < 0.001$, Figure S9). As depicted in Figure 3e-g, it is worth noting that the levels of three pro-inflammatory cytokines presented a similar trend. CeO_2 group, CeO_2 + laser group, and Au@CeO_2 group exhibited a certain degree of decline in the expression of TNF-α, IL-6, and IL-1β. By contrast, Au@CeO_2 + laser group showed dramatically attenuated levels of pro-inflammatory cytokines, which revealed that Au@CeO_2 plus laser played a considerable role in regulating inflammatory cytokines. Overall, these results suggested that Au@CeO_2 owned enhanced ROS scavenging and expression inhibition of pro-inflammatory cytokines functions *in vitro* in the case of laser irradiation.

PPT Effect and Oxygen Generation of Au@CeO_2 Nanoparticles *In Vivo*. We assessed the effectiveness of Au@CeO_2 on CIA mice model, which is the classic model commonly used in RA studies. It was reported that CIA model has striking pathologic features observed in human RA,[54,55] such as inflamed synovium and bone erosion. In the CIA mice model, PAI was utilized to intuitively monitor sO_2 in the blood of ankle joint with intra-articular injection of Au@CeO_2 (Figure 4a). Compared with mice treated with either laser or Au@CeO_2 alone, a strong PA signal was observed in the mice treated with Au@CeO_2 and 808 nm laser irradiation (1 W cm^{-2})

after injection, implying a higher concentration of sO_2. Quantitatively, the sO_2 level increased from 12.3 ± 0.5% to 25.6 ± 0.7% after injection Au@CeO_2 with laser exposure at 30 min (Figure 4b), which indicated that Au@CeO_2 plus laser could immediately and efficiently generate oxygen to ameliorate the hypoxia environment of RA joints.

To investigate the *in vivo* plasmonic photothermal efficacy, the PPT of both AuNR and Au@CeO_2 were performed in CIA mice model. After intra-articular injection of PBS, AuNR, and Au@CeO_2 solutions (1.5 mg kg^{-1}) under the same conditions, thermal images of the inflamed paws and corresponding temperature curves were continuously acquired (Figure 4c,d). As could be seen from the Figure 4c, under localized 808 nm laser irradiation (1 W cm^{-2}) for 5 min, the temperature of inflammatory joint in the Au@CeO_2 group exhibited a rapid rise up to about 55 °C while the temperature was about 51.4 °C in the AuNR group and the control group temperature only slightly rose, which was consistent with the *in vitro* study. The above results proved that Au@CeO_2 had superior photothermal properties *in vivo*.

Therapeutic Effect of Au@CeO_2 Nanoparticles *In Vivo*. Next, the therapeutic efficacy of Au@CeO_2 was evaluated using a CIA murine model. After primary immunization, Balb/c mice bearing CIA were given pre-designed treatments with normal mice as a control. Clinical index (Figure 5a) and ankle thickness (Figure 5b) were employed to reveal clinical outcomes after 28 d of the initial treatment, discreetly recording every 4 d during the observation. As shown in Figure 5a, the clinical index of the paws showed no apparent change among the PBS, PBS + Laser

(1 W cm^{-2}, 5 min), and AuNR three groups even at the study endpoint, indicating that they had no inhibitory effects on joint inflammation. While AuNR + Laser (1 W cm^{-2}, 5 min) group and Au@CeO_2 group partially descended to some extent in the clinical index. By comparison, the mice of Au@CeO_2 + Laser (1 W cm^{-2}, 5 min) group exhibited a significantly lower clinical index than other treated groups, suggesting a pronounced therapeutic effect against RA. Additionally, Figure 5b displayed the changes in ankle thickness measured during treatment. A marked inhibition in the increase of ankle thickness was observed in Au@CeO_2 + Laser therapy group. It is worth mentioning that the CIA mice treated with Au@CeO_2 + Laser exhibited significant body weight gain when compared with other treatment groups within 28 days of treatment. (Figure S10).

Representative photos of the joints and claws of mice in seven groups on the beginning, 14 d, and 28 d of different treatments were displayed in Figure 5c, which provided visualized evidence of the anti-inflammatory effects of Au@CeO_2 compared with the mice in other treatment groups. Subsequently, we further assessed bone destruction of the paws in the seven mice groups using micro-computed tomography (micro-CT) 28 days after treatments (Figure 5d). Micro-CT images showed bone erosion in a certain degree was partially alleviated in the Au@CeO_2 group and AuNR + Laser group. By contrast, the ankle and finger joints of Au@CeO_2 + Laser group exhibited absolutely elimination of bone erosion, indicating more effective bone erosion inhibition. Then bone mineral density (BMD) and bone volume/total volume (BV/TV) were measured to quantitate the degree of bone destruction in the ankle

joints (Figure S11). Both BMD and BV/TV of Au@CeO_2 + Laser group were significantly higher than those of other treatment groups, illustrating a better protective effect on bone.

We further examined the therapeutic effect of Au@CeO_2 combined with laser irradiation by histological and immunohistochemical analyses after 28 days of treatment (Figure 6a). Synovial inflammation and cartilage destruction are typical pathological features of RA. Hematoxylin and eosin (H&E) staining of ankle joints revealed inflammatory cell infiltration, synovial hyperplasia, and enlarged joint space in the PBS, PBS + Laser, and AuNR three groups. The mice in Au@CeO_2 and AuNR + Laser groups showed partial mitigation in signs of inflammation. Impressively, Au@CeO_2 + Laser group showed no apparent inflammatory response in the synovium, which illustrated that RA was restored to normal status. Identical results were acquired by safranin-O staining. Cartilage destruction was significantly attenuated in the Au@CeO_2 + Laser treatment group. The greatly reduced pathological score of synovial inflammation and cartilage erosion was obtained in the joints treated with Au@CeO_2 and laser (Figure S12). In addition, pro-inflammatory cytokines, including TNF-α, IL-6, and IL-1β, are another crucial indices of therapeutic efficacy. Immunohistochemical staining showed the expression of the three pro-inflammatory cytokines were markedly restrained in the mice treated with Au@CeO_2 plus laser irradiation group compared with other experimental groups (Figure 6a and Figure S12). On the whole, these results demonstrated that Au@CeO_2 and laser irradiation combined treatment exhibited a superior therapeutic outcome against RA.

The Inhibitory Effect of Au@CeO_2 Nanoparticles on Pro-inflammatory Cytokines and HIF-1α *In Vivo*. Pro-inflammatory cytokines and HIF-1α are typical indicators in the pathogenesis of RA, which were abundant in RA articular tissues. The interaction between the pro-inflammatory cytokines triggered the processes of inflammatory and bone destruction, and HIF-1α expression exacerbated synovial inflammation in RA joints.[56,57] Western blot analysis was utilized to analyze protein expression of HIF-1α and pro-inflammatory cytokines (TNF-α, IL-6, and IL-1β) (Figure 6b), which exhibited high expression in CIA-induced mice. Notably, Au@CeO_2 plus laser irradiation significantly reduced the expression levels of HIF-1α, TNF-α, IL-6, and IL-1β, respectively. Subsequently, the effect of Au@CeO_2 on HIF-1α and pro-inflammatory cytokines in the articular tissue was further measured by RT-PCR analysis. As shown in Figure 6c, compared with Au@CeO_2 group, the mRNA expression of HIF-1α was notably suppressed in Au@CeO_2 + Laser group ($p < 0.01$). The result revealed that Au@CeO_2 under laser irradiation ameliorated the hypoxia in RA joints. In addition, similar to the HIF-1α level trend, mRNA levels of TNF-α, IL-6, and IL-1β in the articular tissue were also remarkably abated in Au@CeO_2 + Laser treated CIA mice in contrast to the other groups (Figure 6d-f). To sum up, all these results demonstrated that Au@CeO_2 possessed superior pro-inflammatory inhibition and hypoxic remission properties in RA joints, which might be ascribable to its enhanced anti-inflammatory effect and oxygen generation ability.

CONCLUSIONS

In summary, we successfully fabricated Au@CeO_2 nanoparticles and utilized them for realizing NIR plasmon enhanced heat/oxygen-enriched combination therapy for RA. Under 808 nm laser irradiation, the plasmonic photothermal response of Au@CeO_2 effectively induced inflammatory cell death in arthritic tissues, inhibiting the secretion of proinflammatory cytokines. In the meantime, the high temperature caused by the photothermal effect further strengthened the oxygen-generating catalytic reaction of ceria. Oxygen enrichment significantly ameliorated the hypoxic microenvironment in RA joints, down-regulating the expression of HIF-1α. Finally, inflammation and bone erosion were gradually and absolutely eliminated. Taken together, Au@CeO_2 mediated heat/oxygen-enriched strategy displays great attractive therapeutic potential against RA joints. This will not only open up a new pathway to triumph over the excruciating autoimmune diseases, but also provide a novel idea for the design of CeO_2-based anti-inflammatory nanosystems.

EXPERIMENTAL SECTION

Materials. Ultrapure water was obtained from a Milli-Q system. All chemicals were certified of analytical reagent grade and used without further purification. Gold (III) chloride trihydrate ($HAuCl_4$, > 98%), sodium borohydride ($NaBH_4$), L-ascorbic acid (AA), hydrochloric acid (HCl), sodium hydroxide (NaOH), hydrogen peroxide (H_2O_2), ammonium hydroxide ($NH_3 \cdot H_2O$), 3-(4,5-Dimethylthiazol-2-yl)-2,5-diphenyltetrazolium bromide (MTT) were purchased

from Sigma-Aldrich. Hexadecyl trimethylammonium bromide (CTAB, 99%), silver nitrate ($AgNO_3$), cerium (III) nitrate hexahydrate ($Ce(NO_3)_3 \cdot 6H_2O$), ethylenediaminetetraacetic acid (EDTA), methoxy–PEG–thiol (mPEG-SH) were purchased from Aladdin.

Synthesis of Au@CeO_2 Nanoparticles. Au nanorods were synthesized by the silver ion-assisted seed-mediated method with some modifications of the previous report.[48-50] Primarily, 10 mL of the as-grown AuNRs solution was centrifuged at 12 000 rpm for 20 min and then redistributed into 8 mL of CTAB solution (0.025 M). Then, 0.8 mL of EDTA-NH_3 solution and 0.08 mL of $Ce(NO_3)_3$ (0.1 M) were added to the dispersion. The resulting solution was shaken for 2 min and then placed it in a 90 °C oil bath for 5-6 h. The CeO_2-coated AuNR product was centrifuged at 5500 rpm for 30 min. Finally, 10 mL of mPEG-SH solution (4 mM) was added into 8 mL of the as-prepared Au@CeO_2 NPs solution, followed by stirring for 2 h. Au@CeO_2-PEG NPs were separated from the solution by centrifugation at 6000 rpm for 20 min.

Characterization. Size and morphology of the nanoparticles were analyzed using a high-resolution transmission electron microscope (HRTEM, JEM-1400) operated at 200 kV. SEM imaging was determined on a FEI Quantum 400F microscope at an acceleration voltage of 20 kV. UV−vis−NIR absorption spectra were recorded using a spectrophotometer (UV-1750) (Shimadzu, Kyoto, Japan). The hydrodynamic diameter was measured by a Zetasizer Nano-ZS (Malvern Instruments). The powder XRD patterns were acquired on an AXS D8 advance (Bruker, Germany). Metal ion concentration analyses were carried out on an inductively coupled plasma-mass

spectrometry (ICP-MS) (Thermo Fischer Scientific iCAP-QC). An optical fiber-coupled 808 nm laser (SBT Beijing Co., Ltd., China) was used to achieve photothermal increasing temperature.

Photothermal Effect of Nanoparticles. Firstly, the solutions of 200 μg mL^{-1} of AuNR, CeO_2 and Au@CeO_2 were irradiated under NIR laser (808 nm, 1 W cm^{-2}, SBT Beijing Co., Ltd., China) for 5 min. Simultaneously, the real-time thermal images of the samples were recorded using a thermal camera and quantified using the monitoring software. Then, six concentration gradients of Au@CeO_2 (0, 12.5, 25, 50, 100 and 200 μg mL^{-1}) were irradiated by the 808 nm laser for 5 min. Thermometry probe was served to record the temperature change every 50 s.

H_2O_2 Decomposition Assay. A total of 100 μM of H_2O_2 and 200 μg mL^{-1} of AuNR, CeO_2 and Au@CeO_2 were respectively mixed into PBS in 15 mL centrifuge tubes at room temperature. Under the condition of with or without 808 nm laser irradiation, the H_2O_2 concentration was evaluated using a hydrogen peroxide assay kit by measuring the absorbance of the solution at 405 nm every 10 min to 1 h.

Oxygen Generation Assay. 200 μg mL^{-1} of AuNR, CeO_2 and Au@CeO_2 was dispersed in PBS incorporating 100 μM of H_2O_2 at room temperature. With or without 808 nm laser irradiation, oxygen generation levels were monitored until 1 h using a portable dissolved oxygen meter (JPBJ-608) every 10 min. Meanwhile, oxygen bubbles were observed in an Eppendorf tube. In addition, AuNR and CeO_2 were mixed in PBS containing 100 μM of H_2O_2, oxygen production capability of the mixed solution was measured over time by dissolved oxygen meter under 808nm laser

irradiation.

Cytotoxicity Assay. The *in vitro* cytotoxicity was investigated using a standard MTT assay. The RAW 264.7 cells were seeded into 96-well plates and cultured for 24 h. Then, the Au@CeO_2 solutions with different concentrations (0, 12.5, 25, 50, 100 and 200 μg mL^{-1}) were added to the plates and cocultured at 37 °C for 24 h. After that, 10% MTT solution was added and incubated at 37 °C for 4 h. Finally, the MTT solution was removed and 200 μL of DMSO was added to each well to dissolve the action products for 20 min. The OD values were analyzed by measuring the absorbance at 490 nm using a microplate reader.

Enhancement of Photothermal Cytotoxicity *In vitro*. The LPS-induced macrophages RAW 264.7 cells at a density of 5×10^4 cells per cm^2 were cultured in 96-well plates for 24 h. Then the cells were cocultured with AuNR and Au@CeO_2 at different concentrations (0, 12.5, 25, 50, 100 and 200 μg mL^{-1}) for another 24 h, respectively. After that, the cells were washed twice with PBS to remove free nanoparticles and changed the medium to DMEM or PBS. Finally, the cells were irradiated with 808 nm laser (1 W cm^{-2}) for 5 min, and then incubated at 37 °C for 3 h. The photothermal induced cytotoxicity was determined by MTT assay.

The LPS-induced macrophages RAW 264.7 cells were seeded into 96-well plates and incubated at 37 °C for 24 h. Then the cells were randomly divided into six groups and cocultured with PBS, 200 μg mL^{-1} of AuNR, and 200 μg mL^{-1} of Au@CeO_2 for 24 h. After washing twice with PBS to remove excess nanoparticles, three groups of cells were irradiated with 808 nm laser (1 W cm^{-2}) for 5 min, and the other three

groups did not need laser treatment, then incubated for 3 h. To observe the cells enhanced therapeutic effect of Au@CeO_2 intuitively, calcium fluorescein (AM) and PI were used to stain the living and dead cells and the cell images were observed by a laser confocal fluorescence microscope (LCFM, FV1200, Olympus, Tokyo, Japan).

Intracellular H_2O_2 Assay. Intracellular H_2O_2 assay (Sigma-Aldrich) was used to assess the intracellular H_2O_2 concentration. Firstly, a total of 100 μM of H_2O_2 was added to the RAW 264.7 cells, which were pre-incubated with 200 μg mL^{-1} of CeO_2 and Au@CeO_2 for 24 h. Secondly, after 808 nm laser irradiation for 5 min, the cells continued to be incubated for another 3 h. Ultimately, the cell culture medium was replaced by PBS, and the concentration of H_2O_2 in the cell was measured by fluorescence hydrogen peroxide detection kit (ex/em = 490/520 nm).

Intracellular Inflammatory Cytokines Assay. The concentrations of TNF-α, IL-6, and IL-1β in RAW 264.7 cells culture supernatants were determined by TNF-α, IL-6, and IL-1β ELISA kits (Shanghai Neobioscience Technology Co., Ltd., China) according to the manufacturer's instructions.

PAI Performance of Nanoparticles. To test the linearity of PA signals, six concentration gradients of the solutions of AuNR, CeO_2 and Au@CeO_2 were employed for PA signals detection, respectively. In RA model mice, intraarticular injection of PBS, AuNR and Au@CeO_2 at the same concentration (200 μL, 1 mg kg^{-1}). PA signals were utilized for monitoring the movement of nanoparticles in inflammatory joints at different time points. Total PAI datum of these samples were collected by a commercial Vevo LAZR system (FUJIFILM VisualSonics, Toronto,

Canada), and the value of the PA signal was gained by partitioning the region of interest (ROI). 3D reconstruction PA images of the arthritis paws tracked the distribution of nanoparticles dynamically.

Collagen-Induced Arthritis Model. All animal experiments were carried out in compliance with the guidelines of the Institutional Animal Care and Use Committee of Xiamen University. Male 7- to 8- week-old Balb/c mice were used for establishing CIA model. Bovine type II collagen (CII) was dissolved in 0.05 M glacial acetic acid at 4 °C overnight with total concentration of 2 mg mL^{-1}. Then, the CII was fully emulsified with an equal volume of complete Freund's adjuvant (CFA). The right hind limbs of Balb/c male mice were sterilized with 75% alcohol, and the primary immunization was carried out by injecting 50 μL CII emulsion into the middle skin of mouse foot about 3 cm away from the joint. Next, a booster injection of 25 μL of CII emulsified in incomplete Freund's adjuvant (IFA) was given to mice at 21 days after the primary immunization.

PAI of Oxygen Levels in Ankle Joint. A commercial Vevo LAZR system (FUJIFILM VisualSonics, Toronto, Canada) was utilized for investigating vascular sO_2 in the ankle joint cavity. sO_2 around inflammatory joints in CIA mice model was determined before and after intra-articular injection of 200 μg mL^{-1} of Au@CeO_2 into the joints. After 808 nm laser irradiation, the differential optical absorption of deoxygenated and oxygenated hemoglobin at different wavelength of 750 and 850 nm, respectively, was employed for measuring the levels of sO_2 around inflammatory joints by a Vevo LAZR system.

Combined Therapy of Photothermal and Oxygen Production *in vivo*. CIA model mice were divided randomly into six groups and normal mice set as control group (n=6): (1) control, (2) PBS, (3) PBS + Laser (1 W cm^{-2} for 5 min), (4) AuNR, (5) Au@CeO_2, (6) AuNR+ Laser (1 W cm^{-2} for 5 min), (7) Au@CeO_2+ Laser (1 W cm^{-2} for 5 min). PBS, AuNR and Au@CeO_2 were administered into synovial joints via intra-articular injection, respectively (200 μL, 1 mg kg^{-1}). Then the paws of the CIA rats were irradiated with an 808 nm laser at 1 W cm^{-2} for 5 min and the temperature change of the paw was carefully recorded by an IR thermal camera every 1 min. Treatment was performed three times a week for a total of four weeks. Clinical index, ankle thickness and body weight were served as indexes to monitor the arthritis disease severity and progression. Clinical index of CIA mice was recorded by evaluating the evidence of erythema and swelling of each paw. The evaluated paws were graded individually from 0 to 4 based on the following scale: score 0 = normal paw; score 1 = erythema and weak swelling of one toe; score 2 = erythema and swelling on more than one toe; score 3 = severe erythema and swelling of the entire paw; score 4 = complete erythema and swelling of the whole paw and ankle. Then the ankle thickness and the body weight of mice were gauged every four days via a digital caliper and an electronic scale, respectively.

Micro-CT Analysis. After four weeks of different treatments, the right hind limbs of CIA mice and normal mice were scanned on a 3D microcomputed tomography (micro-CT, SkyScan 1178, Bruker, Germany), respectively. Images of paws were gathered under the following scan parameters: tube voltage = 45 kV, tube current =

550 μA, scanning resolution = 18 μm, rotation angle = 360º. Then the scanning images were reconstructed into 3D images using micro-CT software. 3D BMD (mg cm^{-3}) and total bone volume (BV) of the arthritis joints were quantified to analyze the volumetric change of arthritis joints.

Histology Study. The mice were euthanized four weeks after each treatment and collected the right hind limbs for desquamation. Then all specimens were fixed in 10% formalin and decalcified with ethylenediaminetetraacetic acid decalcifying solution for four weeks. Joint tissues were embedded in paraffin, and microcosmically sliced into 5 μm thick paraffin sections for H&E staining or safranin-O staining. To analyze the expression of TNF-α, IL-6, and IL-1β in the inflammatory tissue, ankle joint was stained with specific antibodies directed against TNF-α, IL-6, and IL-1β (Abcam, UK). Peroxidase/dolichos bifows agglutinin (DAB) antibodies were served to the secondary antibody for chromagen development. All images were observed with a light microscope (CX31, Olympus).

qRT-PCR and Western Blot Analysis. Total RNA from the ankle joint of CIA mice or normal mice was extracted by a RNeasy Plus Mini Kit (Qiagen NV, Venlo, the Netherlands). NanoDrop spectrometer (ND-2000, Thermo Fisher Scientific, USA) was used for detecting the RNA concentration and purity. Then conversion of complementary DNA (cDNA) was performed using a reverse transcription kit (Thermo Fisher Scientific, USA) by following the manufacturer's instructions. Eventually, iQ SYBR Green Supermix (Bio-Rad) was added to cDNA to implement the qRT-PCR via the standard protocol.

Western blot analysis was used to evaluate the expression level of protein marker in inflammatory joints. The joint tissues were split by RIPA lysate containing protease inhibitor cocktail, then homogenated at 30000 rpm for 10 min by an electric homogenizer. The supernatants were collected by centrifugation 13000 rpm for 20 min at 4 °C for protein quantification and protein sample preparation, and the protein concentration was determined according to the instructions of BCA protein quantitative kit. After 20 min of electrophoresis at 90 V, the proteins were transferred to a polyvinylidene fluoride (PVDF) membrane (0.45 μm, Millipore, USA). The membranes were blocked with 5% skim milk for 2 h to avoid non-specific binding. Then the membrane was incubated with primary antibodies against HIF-1α, TNF-α, IL-6, and IL-1β (Abcam) for overnight at 4 °C. The dilution ratio of anti-HIF-1α antibody is 1:200, and that of anti-TNF-α, anti-IL-6, anti-IL-1β and actin antibody is 1:1000. Membranes were washed with TBST on the second day and the next day, membranes were washed 3 times with TBS-T and incubated with secondary antibodies conjugated to horseradish peroxidase for 40 min. Blotted membranes were visualized by a Gel Image System ver.4.00 (Tanon, China). Statistical Data Analysis: All statistical analyses were performed using GraphPad Prism v. Five (GraphPad Software Inc., CA, USA). Data were presented as mean ± standard deviation. Significant differences were determined by one-way analysis of variance (ANOVA) and $P < 0.05$ was regarded as statistically significant.

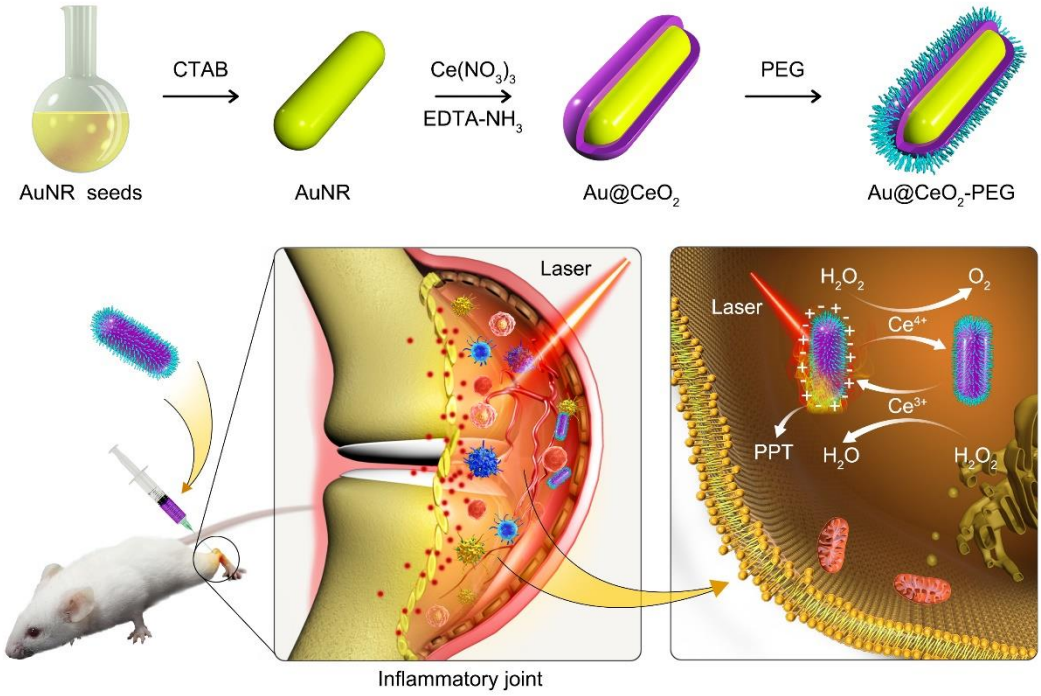

Scheme 1. Schematic diagram showing the preparation and application of $Au@CeO_2$ nanoparticles.

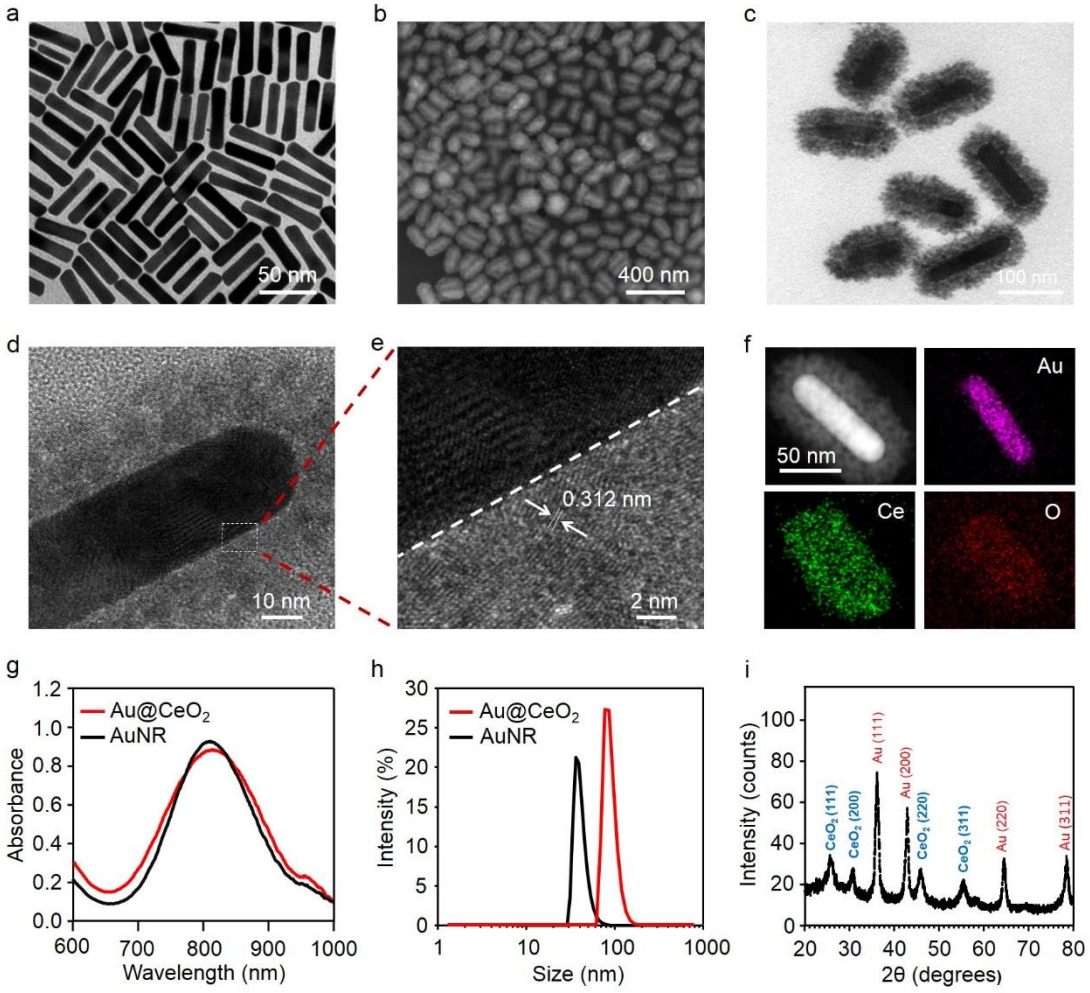

Figure 1. (a) Representative TEM image of AuNRs. (b, c) SEM image and TEM image of Au@CeO_2 NPs. (d) TEM image taken at the end of a single Au@CeO_2 core@shell nanostructure. (e) STEM image of the area marked with a box in (d). (f) HAADF-STEM image of a single Au@CeO_2 and corresponding EDX elemental mapping images of Au, Ce, and O, respectively. (g) UV–Vis spectra of AuNRs and Au@CeO_2. (h) Hydrodynamic diameter distribution of AuNRs and Au@CeO_2 measured by DLS. (i) XRD patterns of Au@CeO_2.

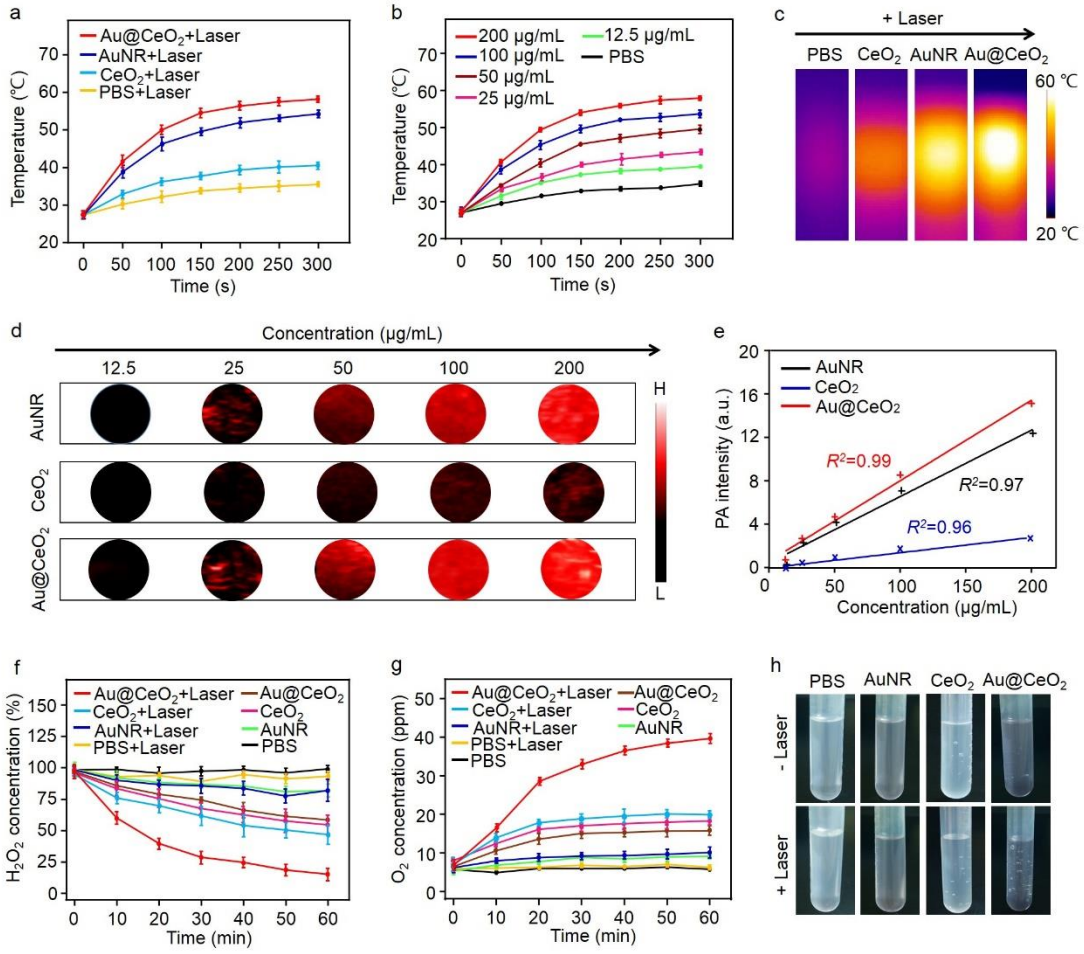

Figure 2. (a) Heating curves of CeO_2, AuNR, and $Au@CeO_2$ solutions with the same concentration of 200 μg mL^{-1} under laser irradiation for 5 min (808 nm, 1 W cm^{-2}). (b) Photothermal effects of $Au@CeO_2$ solution at graded concentrations. (c) Thermal imaging after 5 min laser irradiation. (d) PA images of AuNR, CeO_2, and $Au@CeO_2$ at different concentrations (12.5, 25, 50, 100, and 200 μg mL^{-1} respectively). (e) Linear plots of PA signal as a function of AuNR, CeO_2, and $Au@CeO_2$ concentrations. (f) Degradation curves of H_2O_2 in the presence of AuNR, CeO_2, and $Au@CeO_2$ with or without 808 nm laser irradiation (1 W cm^{-2}). (g) Generation curves of O_2 in 100 μM H_2O_2 solution over time under different conditions. (h) Corresponding photographs of

O_2 bubbles generated after incubation with 100 μM H_2O_2 for 1 h.

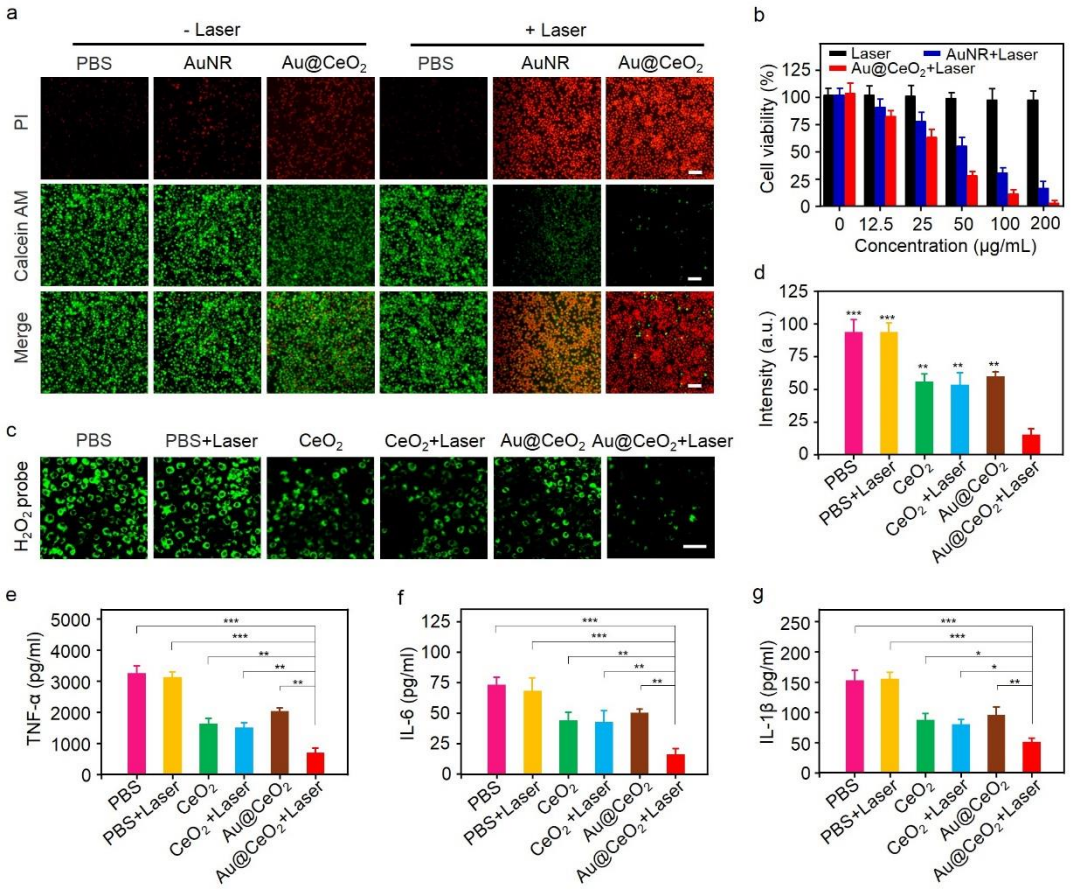

Figure 3. (a) Confocal fluorescence images of LPS-induced RAW 264.7 cells treated with AuNR and Au@CeO_2 after laser irradiation for 5 min (200 μg mL^{-1}, 808 nm, 1 W cm^{-2}). The scale bar is 100 μm. (b) Quantitative results of cell viability treated with AuNR and Au@CeO_2 at different concentrations under 808 nm laser irradiation. (c) CLSM images of H_2O_2 in RAW 264.7 cells treated with CeO_2 and Au@CeO_2 in the presence of H_2O_2. The scale bar is 5 μm. (d) Quantitative fluorescence intensity of intracellular H_2O_2 under laser irradiation. (e-g) Pro-inflammatory cytokines levels of TNF-α, IL-6, and IL-1βin LPS-induced RAW 264.7 cells treated with CeO_2 and Au@CeO_2 with laser irradiation. Data presented as mean ± SD. *$p < 0.05$, **$p < 0.01$, ***$p < 0.001$.

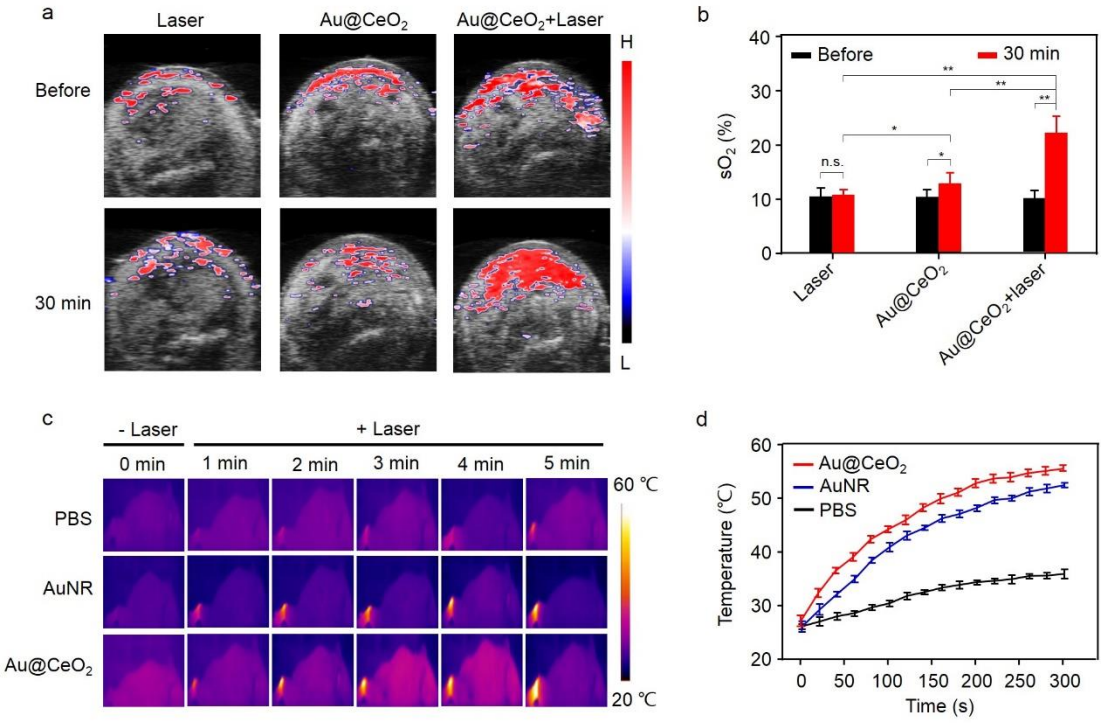

Figure 4. **(**a) PA images of sO_2 in the ankle joint of CIA mice after intra-articular injection of $Au@CeO_2$ with or without laser irradiation (808 nm, 1 W cm^{-2}). Scale bar is 2 mm. (b) Quantification of sO_2 in the ankle joint. (c) IR thermal images of CIA mice at different time points after intra-articular injection of AuNR and $Au@CeO_2$ solutions (1.5 mg kg^{-1}, 50 μL). (d) Corresponding temperature changes in 5 min. Data presented as mean ± SD. *p < 0.05, **p < 0.01, ***p < 0.001, n.s., no significance.

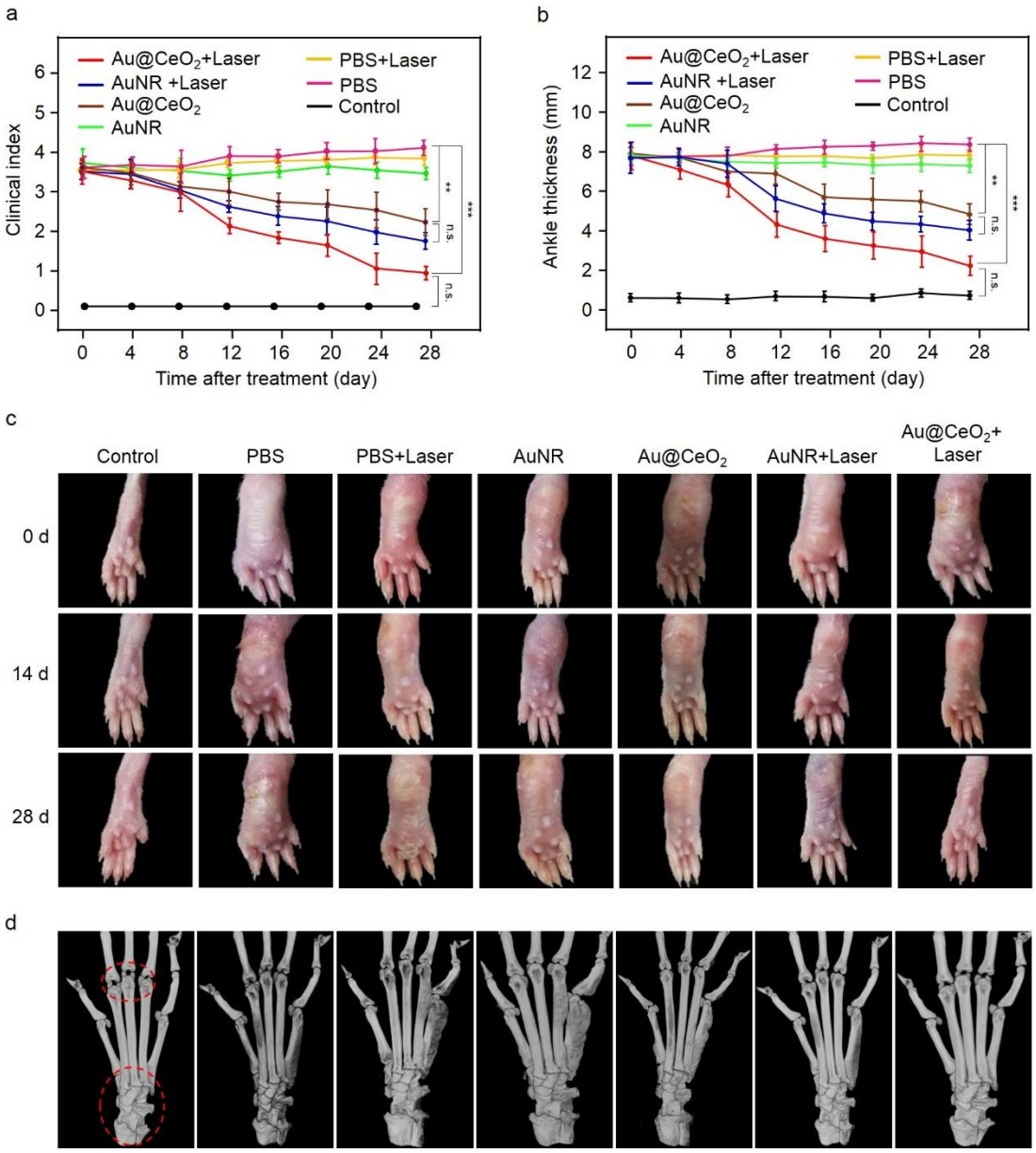

Figure 5. Clinical index (a) and ankle thickness (b) change curves of CIA mice during treatment. (c) Representative photographs of paws of CIA mice on day 0, 14 and 28 under different treatment conditions. (d) Micro-CT images of the arthritis paws and ankle articulations in CIA mice treated with different ways on day 28. Laser: 808 nm, 1 W cm^{-2}. Data presented as mean ± SD. *$p < 0.05$, **$p < 0.01$, ***$p < 0.001$, n.s., no significance.

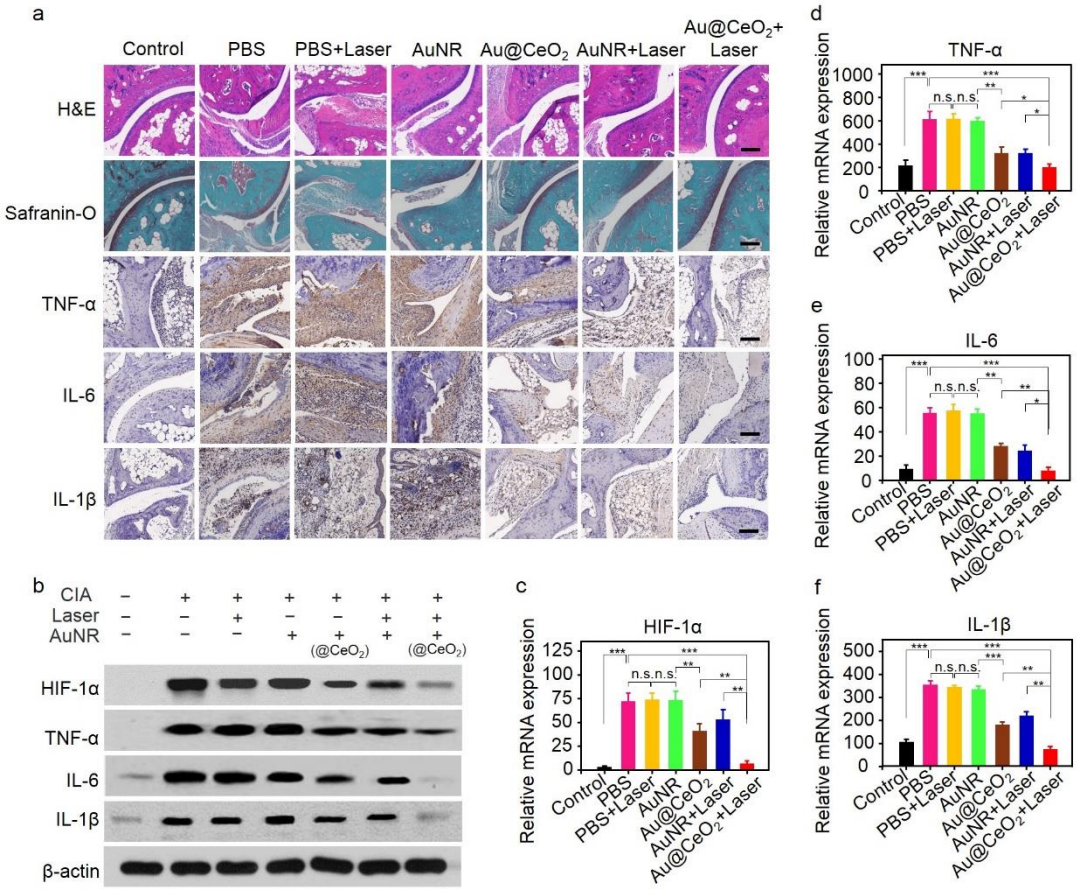

Figure 6. **(**a) Representative images of histological and immunohistochemical staining of ankle joints extracted from mice on 28 days after different treatments. H&E staining for synovial inflammation and safranin-O staining for cartilage erosion. The scale bar is 100 μm. immunohistochemical staining for TNF-α, IL-6, and IL-1β. The scale bar is 50 μm. (b) Protein expression levels of HIF1-α and pro-inflammatory cytokines (TNF-α, IL-6, and IL-1β) measured by Western blot. mRNA expression levels of HIF1-α (c), TNF-α (d), IL-6 (e), and IL-1β (f) in the articular tissue of mice measured by qRT-PCR after 28 days of different treatments. Laser: 808 nm, 1 W cm^{-2}. Data presented as mean ± SD. *$p < 0.05$, **$p < 0.01$, ***$p < 0.001$, n.s., no significance.

ASSOCIATED CONTENT

Supporting Information

Figures showing temperature and linear regression curves, photothermal stability, moving trail of nanoparticles, 3D reconstruction PA images, H_2O_2 degradation curves, concentration-dependent O_2 bubble generation, cell viability, ELISA data analysis, weight change curves, BMD and BV/TV of ankle joints, quantitative analysis of histopathological and immunohistochemical staining

AUTHOR INFORMATION

Corresponding Authors

*E-mail: jxtang0733@163.com.

*E-mail: nielm@xmu.edu.cn.

ORCID

Liming Nie: 0000-0002-1781-4612

Author Contributions

S. W. and R. C. contributed equally to this work.

Notes

The authors declare no competing financial interest.

ACKNOWLEDGMENTS

This work was supported by the National Science Foundation of China (81922034& 91859113), the Science Fund for Distinguished Young Scholars of Fujian Province (2018J06024), the Science Foundation of Fujian Province (No. 2014Y2004), the Natural Science Foundation of Hunan Province of China (2018JJ4061 & 2018JJ4009), the key program of Hunan Provincial Department of science and technology (2016NK2096), and the Scientific Research Fund of Hunan Provincial Education Department (17A055).

REFERENCES

(1) Firestein, G. S. Evolving Concepts of Rheumatoid Arthritis. *Nature* **2003**, *423*, 356-361.

(2) McInnes, I. B.; Schett, G. Pathogenetic Insights from the Treatment of Rheumatoid Arthritis. *Lancet* **2017**, *389*, 2328-2337.

(3) Firestein, G. S.; McInnes, I. B. Immunopathogenesis of Rheumatoid Arthritis. *Immunity* **2017**, *46*, 183-196.

(4) Goulielmos, G. N.; Zervou, M. I.; Myrthianou, E.; Burska, A.; Niewold, T. B.; Ponchel, F. Genetic Data: The New Challenge of Personalized Medicine, Insights for Rheumatoid Arthritis Patients. *Gene* **2016**, *583*, 90-101.

(5) Frisell, T.; Saevarsdottir, S.; Askling, J. Family History of Rheumatoid Arthritis: An Old Concept with New Developments. *Nat. Rev. Rheumatol.* **2016**, *12*, 335-343.

(6) Peters, C.; Morris, C.; Mapp, P.; Blake, D.; Lewis, C.; Winrow, V. The Transcription Factors Hypoxia−Inducible Factor 1α and Ets−1 Colocalize in the

Hypoxic Synovium of Inflamed Joints in Adjuvant−Induced Arthritis. *Arthritis Rheum.* **2004**, *50*, 291-296.

(7) Loeser, R. F. Molecular Mechanisms of Cartilage Destruction: Mechanics, Inflammatory Mediators, and Aging Collide. *Arthritis Rheum.* **2006**, *54*, 1357-1360.

(8) McInnes, I. B.; Schett, G. Cytokines in the Pathogenesis of Rheumatoid Arthritis. *Nat. Rev. Immunol.* **2007**, *7*, 429-442.

(9) Wang, S.; Lv, J.; Meng, S.; Tang, J.; Nie, L. Recent Advances in Nanotheranostics for Treat−to−Target of Rheumatoid Arthritis. *Adv. Healthc. Mater.* **2020**, 1901541-1901558.

(10) Smolen, J. S.; Aletaha, D.; Koeller, M.; Weisman, M. H.; Emery, P. New Therapies for Treatment of Rheumatoid Arthritis. *Lancet* **2007**, *370*, 1861-1874.

(11) Hosaka, S.; Akahoshi, T.; Wada, C.; Kondo, H. Expression of the Chemokine Superfamily in Rheumatoid Arthritis. *Clin. Exp. Immunol.* **1994**, *97*, 451-457.

(12) Brown, B. N.; Ratner, B. D.; Goodman, S. B.; Amar, S.; Badylak, S. F. Macrophage Polarization: an Opportunity for Improved Outcomes in Biomaterials and Regenerative Medicine. *Biomaterials* **2012**, *33*, 3792−3802.

(13) Fearon, U.; Canavan, M.; Biniecka, M.; Veale, D. J. Hypoxia, Mitochondrial Dysfunction and Synovial Invasiveness in Rheumatoid Arthritis. *Nat. Rev. Rheumatol.* **2016**, *12*, 385.

(14) Phull, A. R.; Nasir, B.; ul Haq, I.; Kim, S. J. Oxidative Stress, Consequences and Ros Mediated Cellular Signaling in Rheumatoid Arthritis. *Chem-Biol Interact.* **2018**, *281*, 121-136.

(15) Bae, Y. S.; Lee, J. H.; Choi, S. H.; Kim, S.; Almazan, F.; Witztum, J. L.; Miller, Y. I. Macrophages Generate Reactive Oxygen Species in Response to Minimally Oxidized Low-Density Lipoprotein: Toll-Like Receptor 4- and Spleen Tyrosine Kinase-Dependent Activation of Nadph Oxidase 2. *Circ. Res.* **2009**, *104*, 210-218.

(16) Lu, X.; Chen, R.; Lv, J.; Xu, W.; Chen, H.; Ma, Z.; Huang, S.; Li, S.; Liu, H.; Hu, J. High-Resolution Bimodal Imaging and Potent Antibiotic/Photodynamic Synergistic Therapy for Osteomyelitis with a Bacterial Inflammation-Specific Versatile Agent. *Acta Biomater.* **2019**, *99*, 363-372.

(17) Mittal, M.; Siddiqui, M. R.; Tran, K.; Reddy, S. P.; Malik, A. B. Reactive Oxygen Species in Inflammation and Tissue Injury. *Antioxid. Redox Sign.* **2014**, *20*, 1126-1167.

(18) Elshabrawy, H. A.; Chen, Z.; Volin, M. V.; Ravella, S.; Virupannavar, S.; Shahrara, S. The Pathogenic Role of Angiogenesis in Rheumatoid Arthritis. *Angiogenesis* **2015**, *18*, 433-448.

(19) Qian, C.; Yu, J.; Chen, Y.; Hu, Q.; Xiao, X.; Sun, W.; Wang, C.; Feng, P.; Shen, Q. D.; Gu, Z. Light−Activated Hypoxia−Responsive Nanocarriers for Enhanced Anticancer Therapy. *Adv. Mater.* **2016**, *28*, 3313-3320.

(20) Kim, J.; Cho, H. R.; Jeon, H.; Kim, D.; Song, C.; Lee, N.; Choi, S. H.; Hyeon, T. Continuous O_2-Evolving $MnFe_2O_4$ Nanoparticle-Anchored Mesoporous Silica Nanoparticles for Efficient Photodynamic Therapy in Hypoxic Cancer. *J. Am. Chem. Soc.* **2017**, *139*, 10992-10995.

(21) Wei, J.; Li, J.; Sun, D.; Li, Q.; Ma, J.; Chen, X.; Zhu, X.; Zheng, N. A Novel

Theranostic Nanoplatform Based on Pd@ Pt−PEG−Ce6 for Enhanced Photodynamic Therapy by Modulating Tumor Hypoxia Microenvironment. *Adv. Funct. Mater.* **2018**, *28*, 1706310.1-1706310.12.

(22) Wang, Y.; Xie, Y.; Li, J.; Peng, Z. H.; Sheinin, Y.; Zhou, J.; Oupický, D. Tumor-Penetrating Nanoparticles for Enhanced Anticancer Activity of Combined Photodynamic and Hypoxia-Activated Therapy. *ACS nano* **2017**, *11*, 2227-2238.

(23) Fan, W.; Bu, W.; Shen, B.; He, Q.; Cui, Z.; Liu, Y.; Zheng, X.; Zhao, K.; Shi, J. Intelligent MnO_2 Nanosheets Anchored with Upconversion Nanoprobes for Concurrent pH−/H_2O_2−Responsive UCL Imaging and Oxygen−Elevated Synergetic Therapy. *Adv. Mater.* **2015**, *27*, 4155-4161.

(24) Prasad, P.; Gordijo, C. R.; Abbasi, A. Z.; Maeda, A.; Ip, A.; Rauth, A. M.; DaCosta, R. S.; Wu, X. Multifunctional albumin-MnO_2 Nanoparticles Modulate Solid Tumor Microenvironment by Attenuating Hypoxia, Acidosis, Vascular Endothelial Growth Factor and Enhance Radiation Response. *ACS Nano* **2014**, *8*, 3202-3212.

(25) Zhu, W.; Dong, Z.; Fu, T.; Liu, J.; Chen, Q.; Li, Y.; Zhu, R.; Xu, L.; Liu, Z. Modulation of Hypoxia in Solid Tumor Microenvironment with MnO_2 Nanoparticles to Enhance Photodynamic Therapy. *Adv. Funct. Mater.* **2016**, *26*, 5490-5498.

(26) Chen, Q.; Feng, L.; Liu, J.; Zhu, W.; Dong, Z.; Wu, Y.; Liu, Z. Intelligent Albumin-MnO_2 Nanoparticles as pH-/H_2O_2-Responsive Dissociable Nanocarriers to Modulate Tumor Hypoxia for Effective Combination Therapy. *Adv. Mater.* **2016**, *28*, 7129-7136.

(27) Ma, Z.; Jia, X.; Bai, J.; Ruan, Y.; Wang, C.; Li, J.; Zhang, M.; Jiang, X. MnO_2

Gatekeeper: An Intelligent and O-2-Evolving Shell for Preventing Premature Release of High Cargo Payload Core, Overcoming Tumor Hypoxia, and Acidic H_2O_2-Sensitive MRI. *Adv. Funct. Mater.* **2017**, *27*, 1604258.1-1604258.12.

(28) Wang, S.; Huang, P.; Nie, L.; Xing, R.; Liu, D.; Wang, Z.; Lin, J.; Chen, S.; Niu, G.; Lu, G.; Chen, X. Single Continuous Wave Laser Induced Photodynamic/Plasmonic Photothermal Therapy Using Photosensitizer-Functionalized Gold Nanostars. *Adv. Mater.* **2013**, *25*, 3055-3061.

(29) Song, G.; Liang, C.; Yi, X.; Zhao, Q.; Cheng, L.; Yang, K.; Liu, Z. Perfluorocarbon-Loaded Hollow Bi_2Se_3 Nanoparticles for Timely Supply of Oxygen Under Near-Infrared Light to Enhance the Radiotherapy of Cancer. *Adv. Mater*. **2016**, *28*, 2716-2723.

(30) Dickerson, E. B.; Dreaden, E. C.; Huang, X.; El-Sayed, I. H.; Chu, H.; Pushpanketh, S.; McDonald, J. F.; El-Sayed, M. A. Gold Nanorod Assisted near-Infrared Plasmonic Photothermal Therapy (PPT) of Squamous Cell Carcinoma in Mice. *Cancer Lett.* **2008**, *269*, 57-66.

(31) Huang, X.; El-Sayed, I. H.; Qian, W.; El-Sayed, M. A. Cancer Cell Imaging and Photothermal Therapy in the Near-Infrared Region by Using Gold Nanorods. *J. Am. Chem. Soc.* **2006**, *128*, 2115-2120.

(32) Aioub, M.; Panikkanvalappil, S. R.; El-Sayed, M. A. Platinum-Coated Gold Nanorods: Efficient Reactive Oxygen Scavengers That Prevent Oxidative Damage toward Healthy, Untreated Cells During Plasmonic Photothermal Therapy. *ACS nano* **2017**, *11*, 579-586.

(33) Huang, W.; Chen, R.; Peng, Y.; Duan, F.; Huang, Y.; Guo, W.; Chen, X.; Nie, L. In Vivo Quantitative Photoacoustic Diagnosis of Gastric and Intestinal Dysfunctions with a Broad pH-Responsive Sensor. *ACS nano* **2019**, *13*, 9561-9570.

(34) Cheng, S. J.; Lovell, J. F.; Chen, J.; Gang, Z. Ablation of Hypoxic Tumors with Dose-Equivalent Photothermal, but Not Photodynamic, Therapy Using a Nanostructured Porphyrin Assembly. *Acs Nano* **2013**, *7*, 2541-2550.

(35) Zhou, H. P.; Wu, H. S.; Shen, J.; Yin, A. X.; Sun, L. D.; Yan, C. H. Thermally Stable Pt/CeO_2 Hetero-Nanocomposites with High Catalytic Activity. *J. Am. Chem. Soc.* **2010**, *132*, 4998-4999.

(36) Soh, M.; Kang, D. W.; Jeong, H. G.; Kim, D.; Kim, D. Y.; Yang, W.; Song, C.; Baik, S.; Choi, I. Y.; Ki, S. K. Ceria–Zirconia Nanoparticles as an Enhanced Multi−Antioxidant for Sepsis Treatment. *Angew. Chem., Int. Ed.* **2017**, *129*, 11557-11561.

(37) Kim, J.; Kim, H. Y.; Song, S. Y.; Go, S. H.; Sohn, H. S.; Baik, S.; Soh, M.; Kim, K.; Kim, D.; Kim, H. C. Synergistic Oxygen Generation and Reactive Oxygen Species Scavenging by Manganese Ferrite/Ceria Co-Decorated Nanoparticles for Rheumatoid Arthritis Treatment. *ACS nano* **2019**, *13*, 3206-3217.

(38) Karakoti, A.; Singh, S.; Dowding, J. M.; Seal, S.; Self, W. T. Redox-Active Radical Scavenging Nanomaterials. *Chem. Soc. Rev.* **2010**, *39*, 4422-4432.

(39) Kwon, H. J.; Cha, M. Y.; Kim, D.; Kim, D. K.; Soh, M.; Shin, K.; Hyeon, T.; Mook-Jung, I. Mitochondria-Targeting Ceria Nanoparticles as Antioxidants for Alzheimer's Disease. *ACS nano* **2016**, *10*, 2860-2870.

(40) Lin, W.; Huang, Y. W.; Zhou, X. D.; Ma, Y. Toxicity of Cerium Oxide Nanoparticles in Human Lung Cancer Cells. *Int. J. Toxicol.* **2006**, *25*, 451-457.

(41) Alkilany, A. M.; Thompson, L. B.; Boulos, S. P.; Sisco, P. N.; Murphy, C. J. Gold Nanorods: Their Potential for Photothermal Therapeutics and Drug Delivery, Tempered by the Complexity of Their Biological Interactions. *Adv. Drug Delivery Rev.* **2012**, *64*, 190-199.

(42) Lohse, S. E.; Murphy, C. J. The Quest for Shape Control: A History of Gold Nanorod Synthesis. *Chem. Mater.* **2013**, *25*, 1250-1261.

(43) Jain, P. K.; Huang, X.; El-Sayed, I. H.; El-Sayed, M. A. Noble Metals on the Nanoscale: Optical and Photothermal Properties and Some Applications in Imaging, Sensing, Biology, and Medicine. *Acc. Chem. Res.* **2008**, *41*, 1578-1586.

(44) Nie, L.; Wang, S.; Wang, X.; Rong, P.; Ma, Y.; Liu, G.; Huang, P.; Lu, G.; Chen, X. In Vivo Volumetric Photoacoustic Molecular Angiography and Therapeutic Monitoring with Targeted Plasmonic Nanostars. *small* **2014**, *10*, 1585-1593.

(45) Cheng, L.; Liu, J.; Gu, X.; Gong, H.; Shi, X.; Liu, T.; Wang, C.; Wang, X.; Liu, G.; Xing, H.; Bu, W.; Sun, B.; Liu, Z. PEGylated WS(2) Nanosheets as a Multifunctional Theranostic Agent for in Vivo Dual-Modal CT/photoacoustic Imaging Guided Photothermal Therapy. *Adv. Mater.* **2014**, *26*, 1886-1893.

(46) Liu, Y.; Kang, N.; Lv, J.; Zhou, Z.; Zhao, Q.; Ma, L.; Chen, Z.; Ren, L.; Nie, L. Deep Photoacoustic/Luminescence/Magnetic Resonance Multimodal Imaging in Living Subjects Using High-Efficiency Upconversion Nanocomposites. *Adv. Mater.* **2016**, *28*, 6411-6419.

(47) Nie, L.; Huang, P.; Li, W.; Yan, X.; Jin, A.; Wang, Z.; Tang, Y.; Wang, S.; Zhang, X.; Niu, G.; Chen, X. Early-stage Imaging of Nanocarrier-Enhanced Chemotherapy Response in Living Subjects by Scalable Photoacoustic Microscopy. *ACS Nano* **2014**, *8*, 12141-12150.

(48) Huang, X.; Neretina, S.; El−Sayed, M. A. Gold Nanorods: From Synthesis and Properties to Biological and Biomedical Applications. *Adv. Mater.* **2009**, *21*, 4880-4910.

(49) Nikoobakht, B.; El-Sayed, M. A. Preparation and Growth Mechanism of Gold Nanorods (NRs) Using Seed-Mediated Growth Method. *Chem. Mater.* **2003**, *15*, 1957-1962.

(50) Ni, W.; Kou, X.; Yang, Z.; Wang, J. Tailoring Longitudinal Surface Plasmon Wavelengths, Scattering and Absorption Cross Sections of Gold Nanorods. *Acs Nano* **2008**, *2*, 677-686.

(51) Roper, D. K.; Ahn, W.; Hoepfner, M. Microscale Heat Transfer Transduced by Surface Plasmon Resonant Gold Nanoparticles. *J. Phys. Chem. C* **2007**, *111*, 3636-3641.

(52) Nicolini, V.; Gambuzzi, E.; Malavasi, G.; Menabue, L.; Menziani, M. C.; Lusvardi, G.; Pedone, A.; Benedetti, F.; Luches, P.; D'Addato, S. Evidence of Catalase Mimetic Activity in Ce^{3+}/Ce^{4+} Doped Bioactive Glasses. *J. Phys. Chem. B* **2015**, *119*, 4009-4019.

(53) Lee, S. S.; Song, W.; Cho, M.; Puppala, H. L.; Nguyen, P.; Zhu, H.; Segatori, L.; Colvin, V. L. Antioxidant Properties of Cerium Oxide Nanocrystals as a Function of

Nanocrystal Diameter and Surface Coating. *ACS nano* **2013**, *7*, 9693-9703.

(54) Staines, N.; Wooley, P. Collagen Arthritis-What Can It Teach Us? *Rheumatology* **1994**, *33*, 798-807.

(55) Trentham, D. E. Collagen Arthritis as a Relevant Model for Rheumatoid Arthritis. Evidence Pro and Con. *Arthritis Rheum.* **1982**, *25*, 911-916.

(56) Bingham, C. O. The Pathogenesis of Rheumatoid Arthritis: Pivotal Cytokines Involved in Bone Degradation and Inflammation. *J. Rheumatol. Suppl.* **2002**, *65*, 3-9.

(57) Jeon, C.; Ahn, J.; Chai, J.; Kim, H.; Bae, E.; Park, S.; Cho, E.; Cha, H.; Ahn, K.; Koh, E. Hypoxia Appears at Pre-Arthritic Stage and Shows Co-Localization with Early Synovial Inflammation in Collagen Induced Arthritis. *Clin. Exp. Rheumatol.* **2008**, *26*, 646-648.